

Simple Hamiltonian dynamics is a powerful quantum processing resource

Akitada Sakurai,^{1,*} Aoi Hayashi,^{2,1,3} W. J. Munro,^{1,3} and Kae Nemoto^{1,3,†}

¹*Okinawa Institute of Science and Technology Graduate University, Onna-son, Okinawa 904-0495, Japan*

²*School of Multidisciplinary Science, Department of Informatics,
SOKENDAI (the Graduate University for Advanced Studies),
2-1-2 Hitotsubashi, Chiyoda-ku, Tokyo 101-8430, Japan*

³*National Institute of Informatics, 2-1-2 Hitotsubashi, Chiyoda-ku, Tokyo 101-8430, Japan*

(Dated: May 24, 2024)

A quadrillion dimensional Hilbert space hosted by a quantum processor with over 50 physical qubits has been expected to be powerful enough to perform computational tasks ranging from simulations of many-body physics to complex financial modeling. Despite few examples and demonstrations, it is still not clear how we can utilize such a large Hilbert space as a computational resource; in particular, how a simple and small quantum system could solve non-trivial computational tasks. In this paper, we show a simple Ising model capable of performing such non-trivial computational tasks in a quantum neural network model. An Ising spin chain as small as ten qubits can solve a practical image classification task with high accuracy. To evaluate the mechanism of its computation, we examine how the symmetries of the Hamiltonian would affect its computational power. We show how the interplay between complexity and integrability/symmetries of the quantum system dictates the performance as quantum neural network.

I. INTRODUCTION

Recent developments in the field of quantum computation have seen processors composed of hundreds of qubits realized which can be used to simulate novel phenomena for a variety of physical, chemical and biological systems, as well solving interesting financial and mathematical problems [1–7]. These processors are large enough that they should be able to generate sufficiently complex quantum dynamics so that they can be used to simulate and explore the nature of quantum many-body physics [8–14]. If such an expectation were feasible, then we could consider whether it would be possible to reverse this process and use a typical many-body system, such as the Ising model, to perform computational tasks? This leads to a very interesting question: would natural quantum dynamics alone be a useful resource for quantum computation? If so, would the common beliefs for the requirements for quantum computation change, such as the necessity of non-integrable systems for quantum machine learning [15] and circular unitary ensemble (CUE) processes for the quantum reservoir [16, 17]? Do the commonly used measures for computational capacity, such as the information processing capacity [18–20] remain appropriate? In this article, we aim to answer these questions by designing a quantum computational model using only the Ising model for its quantum contribution.

To explore and address these questions, we benchmark quantum neural networks using quantum extreme reservoir computation (QERC) [21]. This QERC process as depicted in Fig. 1 is an extreme machine learning model with a quantum reservoir for the middle hidden layer of

nodes. As such the quantum reservoir is the only quantum component in the system. The information present in the quantum reservoir would be extracted and converted to the classical data during the measurement step, which is then fed to the one-layer classical neural network. The quantum reservoir provides a given quantum dynamics, while the total system works as the quantum neural network model with the dual nature associated with the extreme machine learning and reservoir computation. More specifically this is a two-layer neural network with a large node number and no optimization nor control on the recurrent neural network (the reservoir).

Among the various quantum machine learning models, we choose the QERC for this benchmark for several reasons. First and foremost variational quantum algorithms [22–24], which are a class of quantum neural networks, have been extensively studied for quantum phase transitions and determining quantum eigenstates [7, 25, 26]. However these models require the ability to apply a quantum circuit with a parameter which is optimized by classical computation. Furthermore there is a known hard optimization problem [27] to be solved to apply these models, besides the difficulty to implement a quantum circuit to realize a good feature space [28, 29]. Second, quantum reservoir computation [30–36] could be closer to the QERC model, however it was constructed as an quantum extension of classical reservoir computation and designed to analyze temporal data. Quantum extreme learning machine had also been conceptually proposed as an extension of the two-layer neural network to be replaced by a quantum neural network [23, 37]. Although, unlike the concept of the quantum perceptron [38–40], these models could be consistent with quantum mechanics, they are not be suitable as a benchmarking candidate until they show at least one concrete instance where they can demonstrate its capability to achieve a significantly high accuracy.

* akitada.sakurai@oist.jp

† kae.nemoto@oist.jp

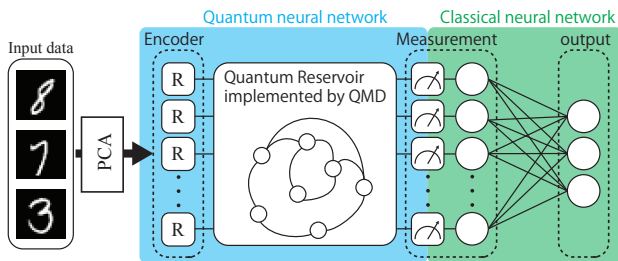


FIG. 1. Schematic illustration of the structure for quantum extreme reservoir computation (QERC). Here the blue and green areas represent the quantum and classical components, respectively. At the first layer, inputs (vectors) are transformed into vectors in a $2N$ -dimensional space using principal component analysis (PCA). These components are then encoded into our quantum system using single qubit rotation gates. Quantum many-body dynamics (QMD), such as the Ising models, maps the input to complex final states. Probability distributions are then obtained at the measurement layer and sent to a single layer classical neural network. The training process is only applied to the classical neural network while the quantum reservoir implemented using QMD is fixed.

By contrast, the QERC model has an explicit form of computation and requires only the initialization of the quantum reservoir to perform various tasks. The (not only conceptual but also) explicit form of the QERC is essential to evaluate the validity of the measures and requirements commonly used for quantum computational capacity. Moreover, it has numerically demonstrated the accuracy necessary for benchmarking with few qubits. This is essential for the numerical evaluation. Now the estimation of the quantum computational power of quantum machine learning models tends to have its focus on the complexity of the quantum process. However, a quantum neural network model provides its capability through the process from the classical input to the classical output. Hence the complexity of the quantum process is not enough to evaluate the capability of the quantum neural network. In the field of computer science benchmarking has long been used for the evaluation of computational capability.

In this paper, we employ benchmarking of the quantum reservoirs within the QERC model to enable us to evaluate the requirements and capacity measures of the quantum reservoir. To achieve this, we must first fix the nature of the output measurements. As such measurements can be as computationally powerful operations, similar to the universality of gate-based quantum computation [41], our measurements in this QERC model will be a projective measurements on to the computational basis. These can be implemented using single qubit Z -axis measurements. Next, the system size in our benchmarking will be around 10 qubits. As such we need to choose an appropriate task to run our benchmarking on, and the MNIST data set for hand-written numbers [42] has a sufficient complexity for this size regime.

II. QUANTUM RESERVOIR MODELS

It is well known that any quantum operation can be decomposed with an arbitrary accuracy with a universal gate set involving only single and two qubit operations [43, 44]. It has been proven that multi-qubit operations are not necessary [43, 44]. However, in Hamiltonian based computation, there is a complexity difference between two-body interactions and those above. In previous work [21], a discrete time crystal model was used corresponding to a multi-body Hamiltonian [21]. It is not therefore clear that two-body Hamiltonian are enough to achieve the same performance in QERC. To evaluate this, let us first employ two Ising models that consist only of one- and two-qubit interactions: the ZZ-Ising model with the corresponding Hamiltonian,

$$\hat{H}_{ZZ} = \hbar \sum_{l>m} J_{lm} \sigma_l^z \sigma_m^z + \hbar g \sum_l \sigma_l^x, \quad (1)$$

and the XX-Ising model given by the Hamiltonian

$$\hat{H}_{XX} = \hbar \sum_{l>m} J_{lm} \sigma_l^x \sigma_m^x + \hbar g \sum_l \sigma_l^z, \quad (2)$$

where σ_l^μ ($\mu = x, y, z$) are the usual spin-1/2 Pauli matrices at the l -th site. Next J_{lm} and $g \geq 0$ are the strength of the two-qubit interaction and the transverse magnetic field, respectively. We set as $J_{lm} = J_0/|l-m|^\alpha$, where J_0 is the strength of the interaction and α a long range order parameter. These Hamiltonians have been experimentally demonstrated in a variety of different physical platforms including [8, 45–51]. In those trapped ions demonstrations [45, 47, 48] $\alpha \sim 1.5$.

Now the XX-Ising and ZZ-Ising models are related by the unitary transformation $\hat{H}_{XX} = \exp(i \sum_l \frac{\pi}{4} \sigma_l^y) \hat{H}_{ZZ} \exp(-i \sum_l \frac{\pi}{4} \sigma_l^y)$. However unlike the situation for the ZZ-interaction, the XX-interaction breaks the $U(1)$ -symmetry meaning the properties and capacity as a quantum reservoir may be different as we observe later.

Next given the XX-Ising and ZZ-Ising models let us consider two further models. The first is the ZZ-X model who dynamics are governed by

$$\hat{U}_{ZZX} = \exp\left(-i\theta_x \sum_l \sigma_l^x\right) \exp\left(-i \sum_{l<m} \theta_{lm}^J \sigma_l^z \sigma_m^z\right) \quad (3)$$

where θ_l^x and θ_{lm}^J are rotation angles. To simplify our analysis further we set $\theta_l^x = \theta_x$ to be equal over the site, similar to the transverse field of the Ising model. Now when $\pi/2 \leq \theta_x < \pi$, the rotation part can be written as,

$$\exp\left(-i \sum_l \theta_l^x \sigma_l^x\right) = \hat{P}_x \exp\left(-i(\theta_x - \pi/2) \sum_l \sigma_l^x\right), \quad (4)$$

where \hat{P}_x is the parity operator. Because \hat{P}_x does not affect the computational basis set (it is a bijection between

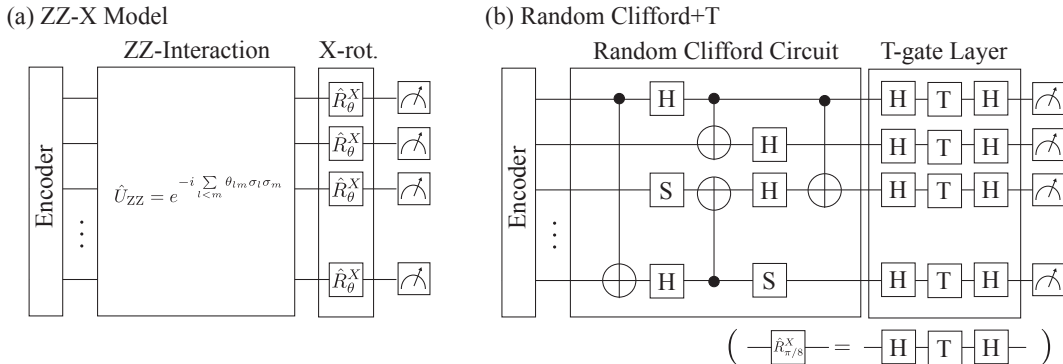


FIG. 2. Depiction of quantum computational circuit for the ZZ-X and Clifford+T models. In (a) for the ZZ-X model, the ZZ-interaction part can be decomposed to a circuit of quantum gates, however it can be advantageous for the ZZ-X model to have the ZZ-interaction part created using Hamiltonian dynamics which would not require any two-qubit gates. As such the simplicity of the model allows one to use more specialized quantum computational devices such as quantum annealer. Next (b) depicts the Clifford+T model where the Clifford circuit consists of only of randomly selected Clifford gates, followed by one layer of T-gates before measurement.

computational basis sets), the performance of $\pi/2 \leq \theta_x < \pi$ will be the same as that of $0 \leq \theta_x - \pi/2 < \pi/2$. Thus, in the analysis, we investigate only the $0 \leq \theta_x \leq \pi/2$ range. Next the angle θ_{lm}^J is site-dependent and like for the Ising model, we consider the long-range interaction to be represented by $\theta_{lm}^J = \theta_J/|l-m|^\alpha$ with θ_J being the maximum angle.

To be more computational complexity oriented, our second additional model is associated with a quantum circuit of the random Clifford gate circuit plus one depth of T-gates for each qubit as the quantum reservoir. Fig. 2 depicts our various strategies where the ZZ-X model has two circuits: the natural dynamics of ZZ-Ising model and the single X rotation on each qubit as seen in Fig. 2 (a). Next Fig. 2 (b) shows the fully gate-decomposed model with random Clifford circuit and the T-gate layer. This is referred to as the Random Clifford+T model in the remainder of this paper.

Finally we employ Haar measure sampling of the unitary matrices as the standard model to evaluate others against. To evaluate this non-trivial dynamics of quantum computation, randomness is often used as an estimator for the computational capability in both experimental demonstrations [13, 52] and quantum variational algorithms [29, 53]. Haar measure sampling has also been used to design quantum machine learning models [16] which are deeply connected to information scrambling in the computational process. The complication in the evaluation here is that the quantum reservoir is not the only element to process the task, that is, the role of the quantum reservoir can change dependent upon the nature of the quantum reservoir. Haar measure random sampling may be ideal for information scrambling, however it is not necessary easy to extract information from such a final state. In quantum algorithms with single-shot projective measurement, information on the quantum computer needs to be scrambled during the process,

however equally needs to be converged to the solution of the problem. In QERC, and more generally any quantum machine learning model, the role of each component is not clear. For instance, usually the circuit before the variational model in VQA is considered for encoding and information scrambling, however that is only a convenient recognition to design the model. Similarly, in QERC it is convenient to think that the quantum reservoir is their to exploit the large Hilbert space indicating information scrambling, however there is no necessity for the model to divide the task in this way. Hence, it is necessary to include Haar measure random sampling in the benchmark to understand the mechanism of the computation.

III. BENCHMARKING

In this benchmarking we will evaluate the quantum reservoir models described in the previous section as they are used in the QERC shown in Fig. 1. It is important to remember that in the QERC model, there are two extra network layers: the encoding of classical data to the quantum reservoir and the measurement of the quantum reservoir. As we use the MNIST hand-written digits (0 to 9) data set for our benchmark, we need to use the principal component analysis (PCA) to encode the $2N$ largest principal components to N spins by single rotations on the initialized state $|0\rangle \otimes \dots \otimes |0\rangle$ as

$$|\psi_l\rangle = \cos(\theta_l/2) |0\rangle + e^{i\phi_l} \sin(\theta_l/2) |1\rangle \quad (5)$$

with $0 \leq \theta_l, \phi_l \leq \pi$ [21]. For each image, the first N elements are encoded on the angles θ_l , while the next N components are encoded on the phase ϕ_l . The smaller components are ignored. In this paper, we consider 10 sites for the Ising model with 10 spins as qubits.

The quantum reservoir readout is achieved by single-qubit projective measurements on the computational basis at the M-layer [21]. The output classical data is then treated and processed by the one-layer classical neural network performing the gradient descent AdaGrad [54] machine learning algorithm as shown in Fig 1 (see appendix A for details on the classical neural network). It is important to note that the M-layer is a middle layer in the neural network of the QERC, and the measurement takes a computational role. In this paper, the computational basis states 0 and 1 are the eigenstates of the Z operator for each qubit.

IV. PERFORMANCE

Let us begin taking the ZZ-Ising model as the quantum reservoir of the QERC to evaluate its performance. Fig. 3 shows the results for the two different strategies with this quantum reservoir. The light blue dots (training) and the light green dots (testing) are for the ZZ Ising model while the blue dots (training) and the green dots (testing) are for the ZZ Ising model with the randomization of single qubit rotation before the time-evolution of the quantum reservoir as shown in the inset (b-2). We have allowed the system to evolve for a scaled time $J_0 t = 3.5$.

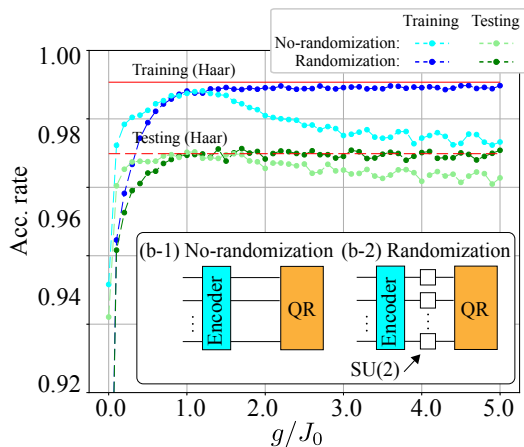


FIG. 3. Plot of the g -dependence of the ZZ-Ising model for a scaled time $J_0 t = 3.5$ in (a) with ten sites, where the transverse magnetic field is applied along the x -axis. The blue and green lines show the training and testing results for the encoder shown in the inset (b-1), while the cyan and light-green lines show the training and testing results for the encoder with random single qubit rotation shown in (b-2).

Although the training accuracy for the Haar measure sampling (indicated as the solid red line in Fig. 3) is slightly better than the highest accuracy with the ZZ Ising model, the highest accuracy with the ZZ-Ising model at $g/J_0 \sim 1$ achieves the accuracy as high as the testing accuracy given by Haar measure random

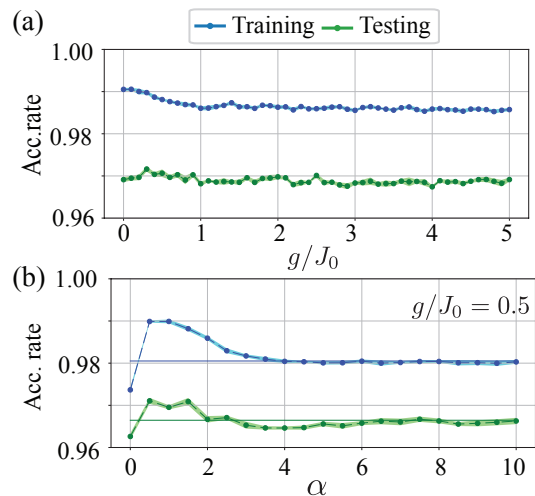


FIG. 4. Plot of the g and α -dependence of the XX-Ising models for a scaled time $J_0 t = 3.5$. Here (a) illustrates the result of the g -dependence with $\alpha = 1.5$ while (b) shows the α -dependence with $g/J_0 = 0.5$. The blue and green dashed lines with dots plot the training and testing accuracy with α ranging from $\alpha = 0.0$ to 10 (the blue and green solid lines indicate the training and testing accuracy with $\alpha = \infty$).

sampling. The degradation of accuracy in the strong transversal magnetic field regime ($g/J_0 > 1$) can be overcome by the randomization of the single qubit rotation. It is worth noting that the single qubit gates alone (without the quantum reservoir) reduces the accuracy rate in this model. This indicates that this process does not directly contribute to the computation, but converts the input state in a form that the quantum reservoir can be more effective. Although the transversal magnetic field is necessary for the QERC to perform, the strong transversal magnetic field introduces the bias in the quantum dynamics, which may cause a mismatch between the tendency in the input data and the quantum reservoir similar to the behavior observed in classical machine learning [55]. Another important aspect of the performance is that the ZZ-Ising model has a superior generalization performance around $g/J_0 \sim 1$.

Next we explore the QERC's performance using the XX-Ising model given in Eq. 2. We begin by showing in Fig. 4 (a) the g -dependence of the XX-Ising model, where we clearly observe that its performance is high even in the $g/J_0 < 1$ regime. That shows that the XX-Ising model can utilize the many-body interaction without the transverse field for computation. The effect of the transverse field appears when we analyze the α -dependence of the performance. The accuracy rates slightly drop for larger g/J_0 when α is large. The best accuracy for large α occurs for $g/J_0 = 0.5$ as shown in Fig. 4 (b).

Now, let us explore our two models that have a quantum circuit structure. Our first evaluation is for the ZZ-X model given by Eq. 3, noting that this model is the exactly the same as the ZZ-Ising model without the

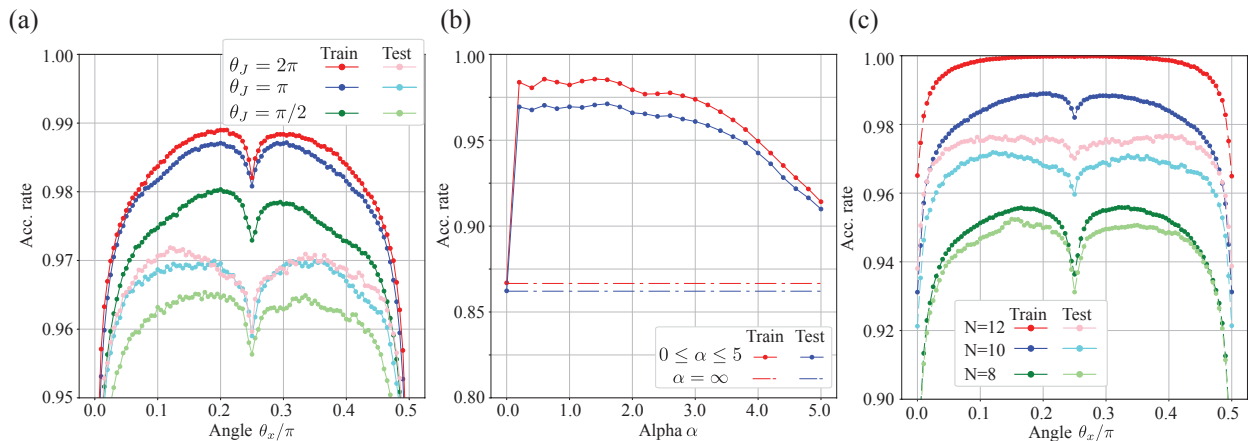


FIG. 5. Classification performance of the ZZ-X model. In (a) we plot the performance with angles $\theta_J = \pi/2, \pi, 2\pi$ and $0 \leq \theta_x \leq 0.5\pi$ for $N = 10$ sites. Then in (b) and (c) we show the α -dependency and size-dependence of the ZZ-X model, respectively. Here we have set $\theta_J = 2\pi$ with $\theta_x = 0.125\pi$ for both plots. The stability of the optimization is shown with shadows to present the standard deviations obtained from 40 to 50 epochs.

transversal field. It is interesting to see if the single qubit rotation is enough to extract the potential complexity generated through the ZZ-Ising interaction. Fig. 5 (a) illustrates the performance of the ZZ-X model dependency on the angle θ_x for each different angle θ_J , while (b) shows the α dependency on the performance. Next (c) shows the performance dependency on the system size for $\theta_J = 2\pi$. The wide range of θ_x, α allows us to achieve high accuracy performance for our classification task.

model	Train acc. (std.)	Test acc.
ZZ-Ising	0.987 ± 0.0004	0.970 ± 0.0006
XX-Ising	0.986 ± 0.0004	0.968 ± 0.0006
ZZ-X	0.986 ± 0.0003	0.972 ± 0.0005
T (HTH)	0.867 ± 0.001	0.8627 ± 0.001
Clifford	0.902 ± 0.001	0.884 ± 0.002
Clifford+T	0.990 ± 0.000	0.970 ± 0.001

TABLE I. Training and testing reservoir accuracy rates for models.

Our second quantum circuit structure model is the Clifford+T model and we present its performance in Table I along with the other models we have considered. We clearly observe that the Clifford+T model has the best performance in terms of both the training and testing accuracy. The ZZ-Ising, XX-Ising and ZZ-X models are however within 0.5%.

V. ENTANGLEMENT AND INTEGRABILITY

Given the above performance benchmarking using the various quantum reservoir models, we now turn our attention to the properties of these quantum reservoirs. Entanglement is known to be necessary for universal quantum computation and is often discussed in quantum machine learning [56]. In the benchmark, all the quantum

reservoirs we evaluated can in general achieve a significantly better performance in a comparison to the performance random single qubit rotations only can provide. All the quantum reservoirs have the power to generate entanglement. As we have seen in quantum computation, entanglement has a certain role in the performance of QERC. However, the reverse statement does not hold, that is, the ZZ-Ising model with $g/J_0 = 0$ does not give any improvement. This may not so surprising, however the comparison of this model with the ZZ-X model gives us an interesting insight. The difference between the ZZ-Ising model with $g/J_0 = 0$ and the ZZ-X model is the last layer of single-qubit gates in the circuit for the ZZ-X model, yet the ZZ-X model can achieve as high as any other quantum reservoir models. Fig. 5 (a) shows the performance (accuracy rate against the single qubit rotation θ_x). The optimal points appear around the angle $\pi/8$, which is equivalent to the T-gate. As we know that single qubit rotations alone cannot contribute to the performance, this indicates that the changing the measurement axis is enough to extract of the entangling dynamics the ZZ-Ising interaction created for the computation. This suggests that the complexity the ZZ-Ising model can generate is sufficient for high QERC performance, which agrees with the XX-Ising models performance noting that the XX and ZZ interactions are related by a simple unitary transformation. A similar behaviour can be seen with the Clifford circuit and the Clifford +T model. This increase of the computational complexity has been reported with Clifford circuit with a single T gate [57], however in our case a single T gate is not enough to fully recover the accuracy rate.

Next, we look into the influence of the integrability of the XX-Ising model on its performance as a quantum reservoir. In the benchmark, we set α to be 1.5, as that parameter value gives the optimal performance. To consider integrability in this case, we take different

values of α to determine how its integrability affects the performance. We will consider three different interaction ranges ($\alpha = 0.0, 1.5$ and ∞). The first $\alpha = 0$ corresponds to all-to-all connectivity with equal strength, whereas $\alpha = \infty$ corresponds to nearest neighbour coupling only. Now $\alpha = 1.5$ sits between these two extremes and corresponds to the long range order parameter present in the recent ion-trap experiments [8, 45, 47, 48]. The training accuracy rates are summarized for these three parameter values in Fig. 6. The best accuracy can be achieved for

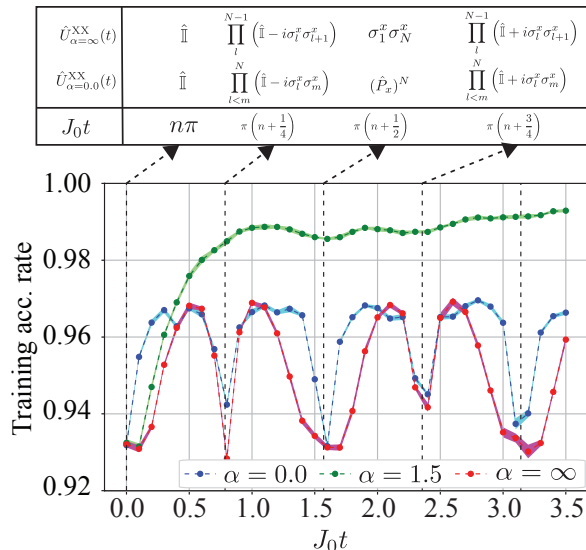


FIG. 6. Plot of the training accuracy rate of XX-Ising model for three different values of $\alpha = 0.0$ (blue), 1.5 (green), ∞ (red). Here we have set $g/J_0 = 0.0$. The shadows displaced show the standard deviations obtained from 40 to 50 epochs. The inset table shows the unitary operators at the stroboscopic times, $J_0 t = n\pi, (n + 1/4)\pi, (n + 1/2)\pi$ and $(n + 1/3)\pi$ with $n \in \mathbb{N}_{\geq 0}$ and where N is the number of sites and \hat{P}_x the parity operator along the x-axis.

a middle range α value. Unlike the case of $\alpha = 1.5$, the $\alpha = 0$ and ∞ cases show periodical behaviour. This reflects to the periodic dynamics of the Hamiltonian with these particular values. It is useful to explore such and mechanics more analytically. Our unitary operator can be decomposed as

$$\begin{aligned} \hat{U}_{\alpha}^{(XX)}(t) &= \exp\left(-i \sum_{l>m}^N \frac{J_0 t}{|l-m|^{\alpha}} \sigma_l^x \sigma_m^x\right) \\ &= \prod_{l>m}^N \left(\cos(\omega_{lm} t) \hat{\mathbb{I}} - i \sin(\omega_{lm} t) \sigma_l^x \sigma_m^x\right), \end{aligned} \quad (6)$$

where the XX-interactions between each site commute with one another. In this case the total unitary can be decomposed as a product of the simple oscillators with the angular frequencies $\omega_{lm} = J_0/|l-m|^{\alpha}$. Thus, when $\alpha = 1.5$, the oscillators are in different angular frequencies. This means the recurrence of dynamics is avoided, resulting in non-periodical dynamics.

Now in the nearest-neighbour interaction case ($\alpha = \infty$), the oscillators may share the same angular frequency introducing a symmetry. Our unitary operator may then be written as

$$\hat{U}_{\alpha=\infty}^{(XX)}(t) = \prod_l^{N-1} \left(\cos(J_0 t) \hat{\mathbb{I}} - i \sin(J_0 t) \sigma_l^x \sigma_{l+1}^x\right) \quad (7)$$

where we observe that the dynamics has a simple analytic form at times $J_0 t = n\pi, (n + 1/4)\pi, (n + 1/2)\pi, (n + 3/4)\pi$ (see the inset table in Fig. 6). This indicates that the unitary starts to grow its complexity over a short period of time, however at some point it starts to saturate and at $J_0 t = n\pi$ its unitary returns to the identity. Consequently, the periodic nature does not allow the system to evolve for times long enough to perform our computation.

It is interesting to also explore the opposite limit of $\alpha = 0$. Here the Ising model also recovers the system symmetry, and the dynamics becomes solvable as

$$\hat{U}_{\alpha=0}^{(XX)}(t) = \prod_{l < m} \left(\cos(J_0 t) \hat{\mathbb{I}} - i \sin(J_0 t) \sigma_l^x \sigma_m^x\right) \quad (8)$$

with all oscillators having the same angular frequency $\omega_{lm} = J_0$. Thus, similar to $\alpha = \infty$, the dynamics is analytic at the times $J_0 t = n\pi, (n + 1/4)\pi, (n + 1/2)\pi, (n + 3/4)\pi$, where its performance reduces, as shown in Fig. 6. When the dynamics is periodical, unless the period is extremely long, it is likely that the dynamics can be fully supported by a small subspace of the Hilbert space. As shown in Fig. 4, the performance quickly recovers as α increases from zero and peaks around $\alpha = 1$, and then gradually decreases to the large α limit. This indicates that the non-integrability of the quantum system contributes to the performance of the quantum neural networks. Interestingly, the power to generate entanglement is not sufficient to estimate the QERC performance as we have seen in above with $\hat{U}_{\alpha=\infty}^{(XX)}$ at $J_0 t = (n + 1/4)\pi$ for instance.

Integrability impacts the performance of the QERC to some degree, however it does not give us clear criteria for the quantum reservoir. The ZZ-X model is an integrable system though it does not hold U(1) symmetry as a result of its time evolution which consists of two Hamiltonian components. This indicates that when the time-evolution has a ‘‘gate’’ structure the integrability may not work as an indicator. This is similar to the case of the Clifford gates + T-gates. The Clifford gate circuit can be efficiently simulated, and does not give us high performance as a quantum reservoir. However the one-depth of T-gates can be enough to achieve similar high performance to the Haar measure sampling. It may not be surprising that the integrability of the Hamiltonian system can significantly affect the performance as quantum neural network. However, the integrability is much less important in the ZZ-X model, which is *integrable* with the analytical form for the output state. Integrability and periodicity are somewhat related in classical dynamics, and as we have seen above, the periodicity in the

Hamiltonian dynamics prevents the states from evolving sufficiently for the one-layer classical neural network to distinguish their distributions. Non-integrability and non-periodicity of the system dynamics are not a necessary condition for a good quantum reservoir, however they can still serve as an indication to provide good neural networks as well as CUE does, which can be useful in designing quantum reservoirs.

VI. INFORMATION SCRAMBLING AND SAMPLING COST

In the previous section, we analyzed the properties of the quantum reservoirs with respect to their complex dynamics. Here, we focus on the other element of quantum computation that can be achieved by quantum reservoir, that is, the convergence to the solution through the quantum algorithm. The quantum dynamics provides a feature space for this computational model, and hence the dynamics complexity is important to deliver information scrambling necessary. To reach a solution, the conversion to it needs to happen, and it is not clear if the quantum reservoir carries the role of information scrambling only or not. If the quantum reservoir somehow contributes to the convergence process, the cost of measurement at M-layer would improve dramatically. To investigate this, we need to estimate the sampling cost for the measurement.

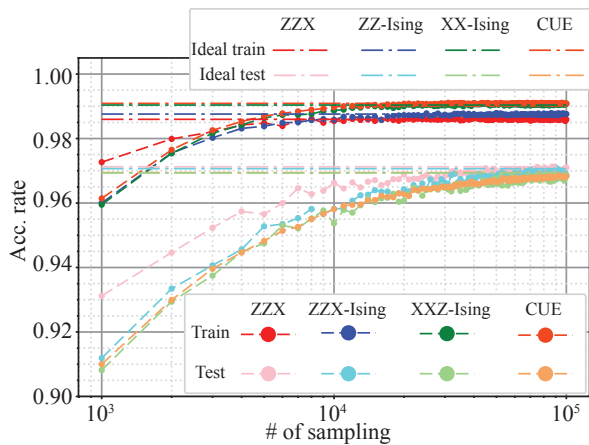


FIG. 7. Sampling cost of QERC using different quantum reservoirs. We plot the sampling number dependence on the performance with the reservoirs (ZZ-Ising, XX-Ising, the Haar random and ZZ-X model), where we set $g/J_0 = 1.0$ for the ZZ-Ising and $g/J_0 = 0.0$ for the XX-Ising model. In both models, we set $J_0 t = 3.5$. The color lines show the accuracy rate for the probability distribution by assuming one can achieve the ideal situation.

The amplitude distribution of the final state of the quantum reservoir was used as the output of the M-layer in our benchmark, however in the simulations we used the amplitude distribution reconstructed from the data. Fig. 7 shows the behaviour of the accuracy rates depen-

dent on the sampling number. All the models in this comparison achieve similar accuracy rates with the theoretical amplitude distribution when the sampling number is large enough. To directly see how well the distribution is reconstructed, we employ the Kullback-Leibler divergence (KLD). Please see Appendix B 2 for more details. In the comparison of these two figures in the Appendix B 2, the accuracy rate converges to the theoretical value before the distributions do. The necessary sampling numbers in the implementation of the QERC are not high in comparison to the dimension of the Hilbert space. In addition, while the cost of the statistical reconstruction of the distribution function is dependent on the size of the computational basis, the necessary sampling number seems less dependent on the size of the computational basis.

Whereas the behaviour of KLD for the different quantum reservoirs remains the same, the ZZ-X model exhibits a different tendency in the small sampling number regime, where it requires a much smaller sampling number than the other models require to achieve the same accuracy (see Appendix B 2). This can not only be a large advantage in its implementation. but also be a hint to consider the trade-off between the information scrambling and the convergence to the classes.

Information scrambling has to happen during the time evaluation of the quantum reservoir. If this is only the role the quantum reservoir carries, the CUE should give the best result. In QERC, the amplitude distribution the M-layer generates has to be fed into the ONN, so if the ONN feels the task to categorize these distribution difficult, the QERC would not achieve a high accuracy rate. The advantage of the ZZ-X model for the sampling number indicates that the distributions the ZZ-X model generates are easier to categorize for the ONN. To examine this ansatz, we investigate the participation ratio in the next section.

VII. PARTICIPATION RATIO (PR)

To evaluate the power of reservoir computation, the Lyapunov exponent and memory capacities such as τ -capacity are widely used: the former being a measure of the chaotic dynamics and nonlinearity in classical reservoirs [58], while the latter are used in classical and quantum reservoir computing [30, 31, 59–62]. The memory capacity is to measure how much past information is stored in the reservoir, and unfortunately such a measure is not appropriate to evaluate the quantum reservoirs used in QERC. Also, to see what is happening in the computational process though the QERC, we need to know what complexity is generated in the state as well as its degree. Hence we employ the participation ratio (PR) used in condensed matter physics to measure the local and extended states [63], such as the Anderson localized and ergodic states, to evaluate the dynamics. For a quantum

state $|\Psi\rangle = \sum_l c_l |l\rangle$, the PR is defined as,

$$\text{PR}(|\Psi\rangle) = \frac{1}{\sum_l |\langle l|\Psi\rangle|^4} = \frac{1}{\sum_l |c_l|^4} \quad (9)$$

where $|l\rangle$ are the computational basis states for our purpose. Importantly, its inverse, so-called inversed PR, has the same form of a quantity used in the analysis of the neuron dynamics [64].

The PR of the output state can be highly dependent on the initial state, and so we considered the averaged PR (APR) over the input state set \mathbb{D} defined by,

$$\text{APR}(\mathbb{D}) = \frac{1}{\#\text{states}} \sum_{|\Psi\rangle \in \mathbb{D}} \left(\frac{1}{\sum_l |\langle l|\Psi\rangle|^4} \right). \quad (10)$$

This value tells us how widely the state is spread over the computational basis on average.

Now if the APR is high, an input state would evolve to an output state supported by many computational basis states. Hence it is more likely that the dynamics yields a strong information scrambling. However a set of such states could be more difficult to categorize by the ONN. If the distribution function reconstructed from the sampling has a distinct feature for each class of the classification task, it would be easy for the ONN to classify these reconstructed distributions, and hence, the sampling number required would be small. To capture such the behavior of all input states contributions, we consider the PR of the mixed states over all inputs, represented by,

$$\hat{\rho}_{\mathbb{D}} = \frac{1}{\#\text{states}} \sum_{|\Psi\rangle \in \mathbb{D}} |\Psi\rangle\langle\Psi|. \quad (11)$$

Then, its PR is obtained by,

$$\text{IAPR}(\mathbb{D}) = \frac{(\#\text{states})^2}{\sum_l \left(\sum_{|\Psi\rangle \in \mathbb{D}} |\langle l|\Psi\rangle|^2 \right)^2}, \quad (12)$$

and we refer to it as the improved APR (IAPR).

Remembering that $\text{APR} \leq \text{IAPR}$, our analysis considers the difference between these defined by $\Delta\text{PR} = \text{IAPR} - \text{APR}$. If the APR is large, IAPR must be large, however when the APR is small, the IAPR can be range from small to large. If the reservoir dynamics creates distributions with a large IAPR but small APR, it might be the optimal output for the ONN to classify. Hence, for our purpose, the measure of our interest is ΔPR .

Before analysing the PRs, we need to take the issue of the bias within the input state set into account. These PR values are dependent on the trend and bias within the set of the input states. In order to evaluate the quantum reservoir neutral to these trends, we introduce two random input sets. First, we consider uniformly distributed points in the 2^N -dimensional space. We generate 10,000 points randomly and use the same encoder as we did

in the benchmark (described in Ref. [21] and the Appendix A 1). The completely random input set is however not so realistic, as the input data set generally has some bias. Hence we also consider a random data set generated by isotropic Gaussian blobs in the high dimensional square with length -10 to 10 (see the sketch in Fig. 8 (b-1)). Here we randomly generate 10,000 points in the high dimensional space. These points form 10 isotropic Gaussian blobs (clusters) where the standard deviation of the clusters is 1.2. These points are mapped to the angles following the encoding process mentioned in Ref. [21] (and Appendix A 1). We also considered the MNIST data set to evaluate the actual practical case (see (c-1) in Fig. 8).

We show the the APR and ΔPR values for the ZZ-Ising model with the benchmark against two random reservoirs: the Haar measure sampling and the single rotation random circuit (SRC). These are given by the red and blue triangles in Fig. 8 respectively. For the ZZ-Ising situation the difference between the randomization of the input state appears in the difference between the red (no randomization) and green (randomization) dots. As the magnetic field strength g increases both the APR and IAPR decrease as shown with the red dots. This agrees with the lower accuracy seen without the randomization for the high g regime. For all of the three data sets, the ZZ-Ising model get close to the value given by the Haar sampling, and hence by taking an optimal parameter values the behaviour of this reservoir is expected to be similar to that of Haar sampling. However, the optimal value for g is not where the APR is the largest. To see this more clearly, we need to investigate the PR values for the ZZ-X model.

The PR values for the ZZ-X model is shown in Fig. 9 with an interesting characteristic being that there are points above the Haar sampling in terms of the APR in the case of the ZZ-X model. Even more interestingly, the optimal point for the QERC performance does not appear near the Haar sampling. The blue dots in these figures show the dependency of the PRs on the single-rotation angle. The optimal point for θ_x in Fig. 5 (c) are near $\pi/8$ meaning the optimal point for this model clearly differs from the point given by Haar sampling. Further the ZZ-X model optimal point is characterized by a lower APR and higher IAPR. For the cases with a lower APR and a higher IAPR, each output distribution function does not broadly spread on the computational basis. This supports the ideal that the ZZ-X model utilize the Hilbert space as much as other models to support the set of the output states however the distribution of each output state is not so flat and hence it is easier for the ONN to distinguish them. This PR ratio and the high performance of the ZZ-X model provides evidence that the ZZ-X model realizes a partial convergence to the classification of the output distributions.

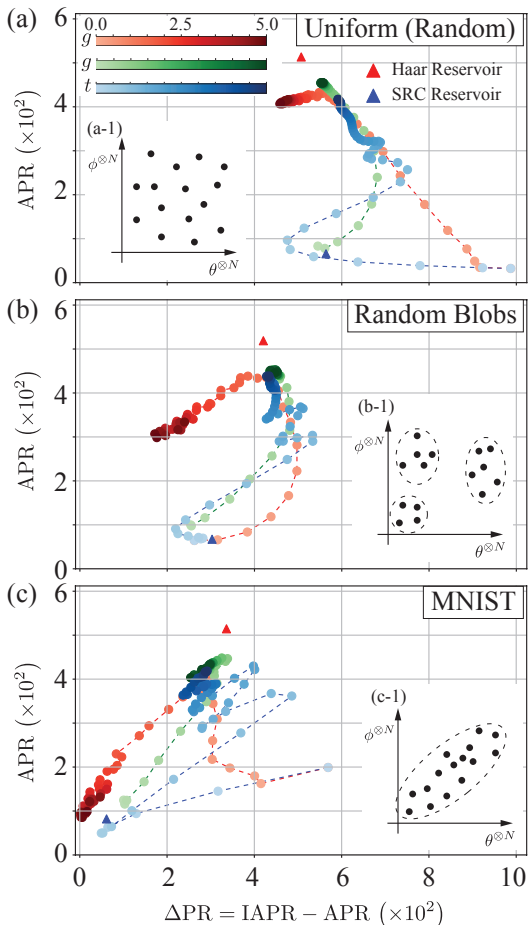


FIG. 8. Plot of the APR vs. ΔPR for ZZ-X-Ising model using ten qubits. The red and green gradation points show the result with different transverse magnetic strengths $0 \leq g/J_0 \leq 5$, where we used normal and randomized encoders in red and green, respectively. Here, we set $J_0 t = 3.5$ with $\alpha = 1.5$. The blue dots show the change of APR and IAPR through the time evolution. The red and blue triangle markers show the results of the Haar and SRC reservoirs. Now (a) and (b) show the results of sets where 10,000 initial states were randomly generated. For (a), all states were created by angles θ_l and ϕ_l that are uniformly randomly generated. Next (b) illustrates the result for the initial state set generated by isotropic Gaussian blobs while (c) depicts the results for the MNIST dataset using 60,000 images.

VIII. DISCUSSION AND CONCLUSION

The analysis in this paper has shown that a Hamiltonian dynamics as simple as ZZ-interaction without the transversal magnetic field can be used to perform non-trivial classical computational tasks. In particular, unlike the previous quantum QERC reservoir [21], no more than two-partite interactions (either physical or effective) are necessary for the QERC to perform. It is well known that the circuit implementation of Haar measure sampling is costly and hence its circuit depth is long.

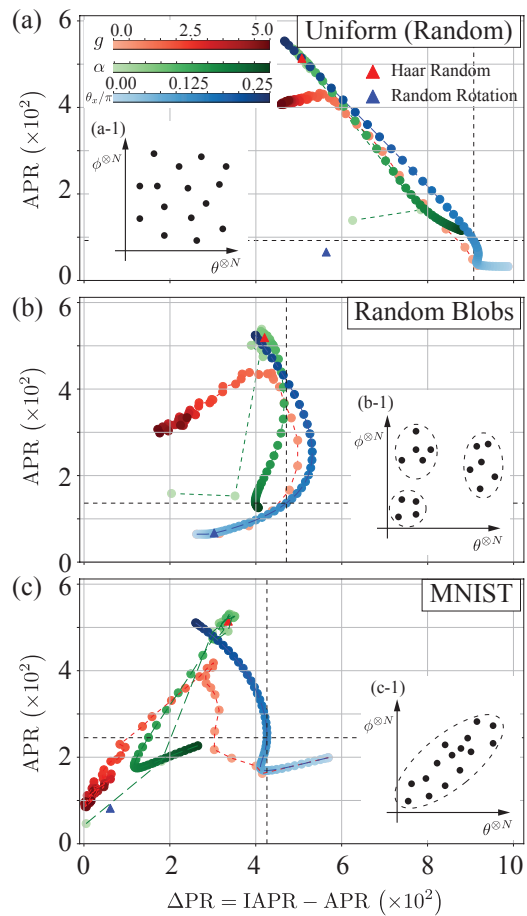


FIG. 9. Plot of the APR vs. ΔPR for the ZZ-X model with ten qubits. The blue line and markers are the results of the ZZ-X model, where we set $0 \leq \theta_x \leq 0.25\pi$, $\theta_J = 2\pi$, and $\alpha = 1.5$. Here, the red line is the result of the ZZ-X-Ising model, where we used the same parameters as in Fig. 8. The green line is the result of the XX-Ising model with $g/J_0 = 0.0$ and $J_0 t = 3.5$. Black dash lines indicate the result of $\theta_x = 0.125\pi$ for ZZ-X model. The red and blue triangle markers show the Haar random and random rotations results. Now (a) and (b) depict the results of the same random initial state sets used in Fig. 8 while (c) shows the results from the MNIST dataset.

The Clifford+T model however achieves similar testing accuracy, which is an advantage when the quantum computation is done in the fault-tolerant manner.

For small scale quantum processing, the Ising models can be implemented in many alternate physical platforms with high accuracy. The sampling measurement cost does not follow the cost associated with the statistical reconstruction of the distribution function, instead scaling well with the size of the computational basis. This is an advantage in the implementation.

Finally the ZZ-X model outperformed the Haar sampled unitary operation in both the testing accuracy and the sampling cost at the measurement, which directly indicates that the generation of the complexity and the use of it would be two different things in designing quan-

tum machine learning systems. Our results have shown a new approach to design quantum-classical hybrid machine learning models as well as given an insight into the computational process within quantum reservoirs.

ACKNOWLEDGMENTS

This work is supported by the MEXT Quantum Leap Flagship Program (MEXT Q-LEAP) under Grant No. JPMXS0118069605, COI-NEXT under Grant No. JPMJPF2221, and the JSPS KAKENHI Grant No. 21H04880.

Appendix A: Quantum Extreme Reservoir Computing (QERC)

Let us provide a detailed description of Quantum Extreme Reservoir Computing (QERC). We start with the general framework used in QERC [21] where we consider an input \mathbf{d} being a D -dimensional vector. We assume this input to be classical, although QERC can be applied to quantum inputs. Now since \mathbf{d} is classical information, it is necessary to encode it onto the initial quantum state $|\psi(\mathbf{d})\rangle_I$ for the quantum reservoir. Through the quantum reservoir dynamics, the initial state $|\psi(\mathbf{d})\rangle_I$ is mapped to the final state $|\psi(\mathbf{d})\rangle_F$ by the unitary operator \hat{U}_{QR} : $|\psi(\mathbf{d})\rangle_F = \hat{U}_{QR}|\psi(\mathbf{d})\rangle_I$.

The final state is then projectively measured into the computational basis, converting the quantum information to classical information. Here, let us define the notation of the computational basis set for the spin system. We take the product states of all the eigenstates of σ_l^z as the computational basis $|x\rangle$, where $|x\rangle \in \{|0\dots 00\rangle, |0\dots 01\rangle, \dots, |1\dots 11\rangle\}$. Because we cannot obtain the amplitude distribution from a single-shot measurement, it is necessary to sample the statistics of the final state. In this model, we use,

$$\mathbf{p}(\mathbf{d}) = \begin{pmatrix} p_1 \\ p_2 \\ p_3 \\ \vdots \\ p_{2^N} \end{pmatrix} = \begin{pmatrix} |\langle 0\dots 00 | \psi_F(\mathbf{d}) \rangle|^2 \\ |\langle 0\dots 01 | \psi_F(\mathbf{d}) \rangle|^2 \\ |\langle 0\dots 10 | \psi_F(\mathbf{d}) \rangle|^2 \\ \vdots \\ |\langle 1\dots 11 | \psi_F(\mathbf{d}) \rangle|^2 \end{pmatrix}, \quad (\text{A1})$$

for all basis $|x_l\rangle$ with $l = 1, \dots, 2^N$. The readout gives us a 2^N -dimensional vector. In our work, the readout is standardized to stabilize the later classical processing: $\mathbf{p}(\mathbf{d}) \rightarrow \mathbf{u}(\mathbf{d})$. In more detail, we employ the standardization given by

$$u_l = \frac{p_l - \bar{p}}{S}, \quad (\text{A2})$$

where $\bar{p} = (\sum_l^{2^N} p_l)/2^N = 1/2^N$ and $S = \sum_l^{2^N} (p_l - \bar{p})^2$ are the mean value and standard deviation, respectively. Next, \mathbf{u} is sent to the classical classifier where we employ the single-perceptron mode (SPM) in which the data

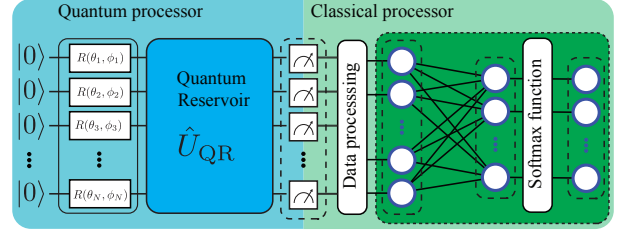


FIG. 10. Schematic diagram of the computational process for Quantum Extreme Reservoir Computing (QERC). The bright-blue and bright-green areas represent the quantum and classical processors, respectively. Classical information is encoded into a quantum system using single qubit rotation gates with angles θ_l, ϕ_l , where $l = (1, 2, \dots, N)$ and N is the total number of qubits of the quantum processor. In QERC, one can use quantum many-body dynamics (QMD), such as the Ising models discussed in the main text, or a quantum gates sequence as a reservoir. Probability distributions are then determined at the measurement layer and sent to a single-layer classical neural network. The training process is only applied to the classical neural network, while the quantum reservoir is fixed.

transfer is given by $\mathbf{y} = f(W\mathbf{x} + \mathbf{b})$. Here \mathbf{y} is the final output of the QERC, W and \mathbf{b} are the weight matrix and bias vector for the SPM. The function $f(\cdot)$ is called an activation function. We employ the softmax activation function [65] in the main text because the QERC is applied to the multi-class classification task. Hence, the final output tells the classification class of the input data.

We use the ‘‘AdaGrad’’ classical algorithms [65] to optimize the weight matrix and bias. It is a gradient descent algorithm that uses landscape information. Our interest here is to apply QERC to image classification. As an illustrative example, we use the MNIST dataset for numerical simulations with 60,000 and 10,000 digits images (28×28 pixels) for training and testing, respectively. The training data prepared in advance has the images \mathbf{d}^{tr} and labels (answers) \mathbf{t}^{tr} recorded in an N_t -dimensional vector. In the optimization process, the AdaGrad minimizes the cost function given by $L = \frac{1}{N_a} \sum_{a=1}^{N_a} \sum_{l=1}^{N_t} t_l^{(a)} \log(y_l^a)$, where N_a is the mini-batch size. This cost function is known as cross-entropy [55].

1. Encode images

Here, we discuss the sampling cost of QERC to perform it properly. Let us explain the encoder part of QERC. The classical input is encoded into the angles of each qubit. The single qubits can be written as,

$$|\psi_1\rangle = \cos \frac{\theta}{2} |0\rangle + e^{i\phi} \sin \frac{\theta}{2} |1\rangle. \quad (\text{A3})$$

where $0 \leq \theta < \pi$ and $0 \leq \phi < \pi$ are the angles. If N -qubits exist, up to $2N$ classical variables can be encoded. However, in the image classification task, such as

digit images of MNIST data discussed in the main text, the input data is an image with more information than $2N$ variables. For example, a digit image (\mathbf{I}) has 28 pixels. In other words, it can be assumed that a vector in a 784-dimensional space: $\mathbf{I} = \sum_{i=1}^{784} c_i \mathbf{e}_i$, where c_i is a pixel value at a basis vector \mathbf{e}_i for $i = 1, 2, \dots, 784$. Thus, in Ref. [21], the Principal Component Analysis (PCA) is used to efficiently decompose images with a new basis set: $\mathbf{I} = \sum_{j=1}^{784} \tilde{c}_j \mathbf{v}_j$, where the j -th element is the j -th contribution among the 784 elements. In the PCA, the new basis vectors are obtained to represent given images efficiently, even using a few basis vectors. It means that there is a priority among the basis. In general, the priority is in the order of $\mathbf{e}_1, \mathbf{e}_2, \dots$, namely, we refer a coefficient \tilde{c}_l of the l -th vector \mathbf{e}_l as l -th principal component. Thus, in the QERC, one encodes the images efficiently using the first few components $l = 1, 2, \dots, 2N$. In more detail, up to N -th component are encoded into θ s of qubits, while from $N + 1$ to $2N$ -th components are encoded into ϕ s of qubits. To map the components to angles, we employ the conversion $\tilde{c}_l \rightarrow \theta_l$ or ϕ_l given by

$$\theta_l \text{ or } \phi_l = \frac{\pi \left(\tilde{c}_l - \min [\tilde{c}_l^{(\text{train})}] \right)}{\max [\tilde{c}_l^{(\text{train})}] - \min [\tilde{c}_l^{(\text{train})}]}, \quad (\text{A4})$$

where $\max [\tilde{c}_l^{(\text{train})}]$ and $\min [\tilde{c}_l^{(\text{train})}]$ are the maximum and minimum values of \tilde{c}_l across all the training samples respectively. In the MNIST classification, $\max [\tilde{c}_l^{(\text{train})}]$ and $\min [\tilde{c}_l^{(\text{train})}]$ are chosen from 60,000 images for training. For images not used in training, such as testing images, we note that when θ_l or ϕ_l goes beyond the range $[0, \pi]$, we truncate the value.

Appendix B: Sampling cost on QERC

1. Estimation of Sampling Number

Let us consider a quantum system with N qubits and run it totally N_s times to estimate the probability distribution. We measure the system with a computational basis set. In other words, for each running, we can get a bit string $x \in \mathbb{S}_N$, where the set \mathbb{S}_N is a set of whole possible N -bits string: $\mathbb{S}_N = \{00 \dots 0, \dots, 11 \dots 1\}$. To simply the discussion, let us assume that we measure a bit string x with $0 \leq N_x \leq N_s$ times. In this assumption, the probability that we get the result is given by

$$P_x(N_x, N_s, p_x) = \frac{N_s!}{N_x!(N_s - N_x)!} p_x^{N_x} (1 - p_x)^{N_s - N_x} \quad (\text{B1})$$

where $p_x = \text{Tr}(\hat{P}_x \hat{\rho})$ is an appearance probability of the string x , and $\hat{P}_x = |x\rangle\langle x|$ is a projection operator along the computational basis state $|x\rangle$ and $\hat{\rho}$ is a quantum state of N -qubits. The expectation value of N_x is given

by

$$\langle N_x \rangle = \sum_{N_x=0}^{N_s} N_x P_x(N_x, N_s, p_x) = N_s p_x, \quad (\text{B2})$$

similarly, its variance is given by,

$$\langle \Delta N_x^2 \rangle = \langle N_x^2 \rangle - \langle N_x \rangle^2 = N_s p_x (1 - p_x). \quad (\text{B3})$$

Now, let us estimate the probability p_x from the above result. As an estimator for p_x , we consider an empirical probability $\tilde{p}_x = N_x/N_s$. Using the $\langle N_x \rangle$ and $\langle \Delta N_x^2 \rangle$, its expectation is given by

$$\langle \tilde{p}_x \rangle = \left\langle \frac{N_x}{N_s} \right\rangle = p_x \quad (\text{B4})$$

its indicates that \tilde{p}_x is the unbiased estimator, and its variance is given by

$$\langle \Delta \tilde{p}_x^2 \rangle = \left\langle \Delta \left(\frac{N_x}{N_s} \right)^2 \right\rangle = \frac{p_x (1 - p_x)}{N_s}. \quad (\text{B5})$$

Thus, its error can be characterized by

$$\epsilon_{\tilde{p}_x} = \sqrt{\langle \Delta \tilde{p}_x^2 \rangle} = \sqrt{\frac{p_x (1 - p_x)}{N_s}}. \quad (\text{B6})$$

As you can see, the error $\epsilon_{\tilde{p}_x}$ is dependent on p_x . As an example, let us consider the two extreme cases. First, let us consider that the probability of the single-bit string x is precisely one. In this case, its error is $\epsilon_L = 0$. Next, consider a case where the probability distribution is uniform: $p_x = 1/2^N$ for arbitral bit string x . Its error can be $\sim 1/\sqrt{2^N N_s}$ for the large N . We see that it becomes small as the number sampling N_s increases. As a state is localized, its estimation error gets smaller. While a state is ergodic, its error gets larger.

It is natural to expect that the stochastic fluctuation of empirical probability may affect the performance of the QERC since the distribution is not the same as the ideal distribution. Thus, here let us see a lower bound of the sampling number N_s using $\epsilon_{\tilde{p}_x}$ for QRCs to get good performance. To estimate it, let us assume a constant factor C , the minimum fluctuation of the probability distribution that affects the classical neural network. Then we get an inequality of $\epsilon_{\tilde{p}_x}$ as follows,

$$\epsilon_{\tilde{p}_x \in \mathbb{S}_N} < C. \quad (\text{B7})$$

In general, finding the proper value of the constant C is difficult, but we can get an estimate of it as follows. After the measurement, the probability distribution is renormalized to have an average zero to the variance one, as follows,

$$q_{x \in \mathbb{S}_N} = \frac{p_{x \in \mathbb{S}_N} - \bar{p}}{\sigma}, \quad (\text{B8})$$

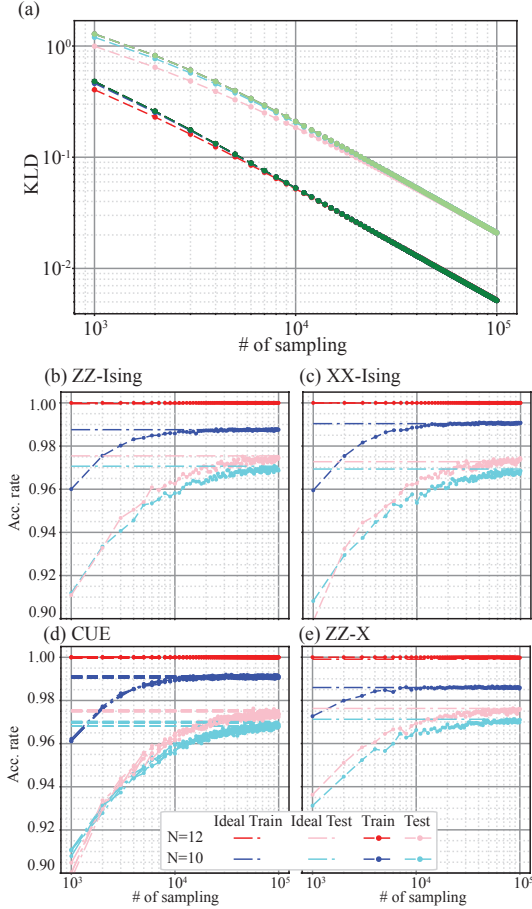


FIG. 11. Plots show the sampling cost of QERC with different quantum reservoirs: (a) show the sampling number dependence on Kullback–Leibler divergence (KLD) for different models with $N = 10$ and $N = 12$. (b)-(e) shows sampling number dependence on the performance with different reservoirs (ZZ-Ising, XX-Ising, the Haar random and ZZ-X model), where we set $g/J_0 = 1.0$ for the ZZ-Ising, $g/J_0 = 0.0$. The color lines show the accuracy rate for the probability distribution by assuming one can get the ideal one. (b) to (e) show the sampling number dependence on the performance for the different reservoirs with $N = 10$ and $N = 12$.

where $\bar{p} = \sum_{x \in \mathbb{S}} p_x$ is mean value, and $\sigma = \sum_{x \in \mathbb{S}} (p_x - \bar{p})^2$ is variance of p_x . It can be written as $\sigma = (\sum_{x \in \mathbb{S}} p_x^2) - 2^{-2N}$. For large systems, because, $2^{-2N} \ll 2^{-N} \leq \sum_{x \in \mathbb{S}} p_x^2$, we assume that $\sigma \approx 1/\text{PR}$. Now, in the new parameter space of p_x , its error can be written as,

$$\epsilon_{q_x} = \text{PR} \cdot \epsilon_{p_x}. \quad (\text{B9})$$

Now, it is natural to assume that when the above error is much smaller than that of the distribution of q_x generated by data, QERC works appropriately. Thus, we assume that the stochastic fluctuation is much smaller than the variance of the normalized distribution, which is one. It can be written as $D \cdot \text{PR} \cdot \epsilon_{p_x} < 1$, where $D \gg 1$ is a constant that relates to a sensitivity of the classical neural network. Finally, consider a case where $\epsilon_{p_x} \sim 1/\sqrt{2^N N_s}$ is the worst case, and the number of shots can be given $D^2 \cdot \text{PR}^2 / 2^N < N_s$. It indicates that the sampling cost is less as the PR is smaller.

For example, when a state is uniformly distributed in the Hilbert space, $\text{PR} \approx 2^N$. Thus, the number of the sampling can be estimated as follows,

$$D^2 \cdot 2^N < N_s \quad (\text{B10})$$

meaning that when $D = 10$, we need at least $N_s = 100 \times 2^N$ sampling to perform QERCs properly.

2. Numerical results with different systems

First, to see the reconstruction performance of the sampling distribution, we calculate the Kullback-Leibler divergence (KLD) between a theoretical distribution and an empirical distribution, which is numerically obtained by random sampling. The results of KLD with different sizes are shown in Fig. 11 (a). It means that as system size increases, one needs more sampling to achieve the same level as is well known.

Next, Figs. 11 (b) to (e) show the difference of the required number of sampling for each quantum reservoir with respect to the number of qubits. There would be a trade off between the advantages (the larger Hilbert space and the larger number of the PCA components) and the disadvantage (the statistical overhead of sampling) for the larger number of qubits. The quantum reservoir with a larger number of qubits would perform better at least at up a certain size in theory due to the larger number of the PCA components can be input and the calculation space is larger, however, due to the reconstruction of the amplitude distribution, it may require a larger number of sampling. The latter can be seen in the small number sampling regime in Figs. 11 (c) and (d). This indicates that the difference between the amplitude distribution to be distinguished is more detailed with these quantum reservoirs. By contrast, the ZZ-X model does not have the region where the smaller quantum reservoir achieves a higher accuracy. This is evidence that the sampling in QERC does not necessarily follow statistical scaling, which is a significant advantage for the implementation.

[1] B. P. Lanyon, J. D. Whitfield, G. G. Gillett, M. E. Goggin, M. P. Almeida, I. Kassal, J. D. Biamonte, M. Mohseni, B. J. Powell, M. Barbieri, *et al.*, Towards

quantum chemistry on a quantum computer, *Nature Chemistry* **2**, 106 (2010).

[2] S. Aaronson and A. Arkhipov, The computational com-

- plexity of linear optics, in *Proceedings of the Forty-Third Annual ACM Symposium on Theory of Computing*, STOC '11 (Association for Computing Machinery, New York, NY, USA, 2011) p. 333–342.
- [3] P. Rebentrost, B. Gupt, and T. R. Bromley, Quantum computational finance: Monte carlo pricing of financial derivatives, *Phys. Rev. A* **98**, 022321 (2018).
 - [4] Y. Nam, J.-S. Chen, N. C. Pienti, K. Wright, C. Delaney, D. Maslov, K. R. Brown, S. Allen, J. M. Amini, J. Apisdorf, *et al.*, Ground-state energy estimation of the water molecule on a trapped-ion quantum computer, *npj Quantum Information* **6**, 33 (2020).
 - [5] A. Carrera Vazquez and S. Woerner, Efficient state preparation for quantum amplitude estimation, *Phys. Rev. Appl.* **15**, 034027 (2021).
 - [6] H. Xu, J. Zhang, J. Han, Z. Li, G. Xue, W. Liu, Y. Jin, and H. Yu, Realizing discrete time crystal in an one-dimensional superconducting qubit chain (2021).
 - [7] M. Gong, H.-L. Huang, S. Wang, C. Guo, S. Li, Y. Wu, Q. Zhu, Y. Zhao, S. Guo, H. Qian, Y. Ye, *et al.*, Quantum neuronal sensing of quantum many-body states on a 61-qubit programmable superconducting processor (2022).
 - [8] J. W. Britton, B. C. Sawyer, A. C. Keith, C.-C. J. Wang, J. K. Freericks, H. Uys, M. J. Biercuk, and J. J. Bollinger, Engineered two-dimensional ising interactions in a trapped-ion quantum simulator with hundreds of spins, *Nature* **484**, 489 (2012).
 - [9] P. Jurcevic, B. P. Lanyon, P. Hauke, C. Hempel, P. Zoller, R. Blatt, and C. F. Roos, Quasiparticle engineering and entanglement propagation in a quantum many-body system, *Nature* **511**, 202 (2014).
 - [10] Q. Guo, C. Cheng, H. Li, S. Xu, P. Zhang, Z. Wang, C. Song, W. Liu, W. Ren, H. Dong, *et al.*, Stark many-body localization on a superconducting quantum processor, *Phys. Rev. Lett.* **127**, 240502 (2021).
 - [11] S. Ebadi, T. T. Wang, H. Levine, A. Keesling, G. Semeghini, A. Omran, D. Bluvstein, R. Samajdar, H. Pichler, W. W. Ho, *et al.*, Quantum phases of matter on a 256-atom programmable quantum simulator, *Nature* **595**, 227 (2021).
 - [12] M. Ippoliti, K. Kechedzhi, R. Moessner, S. Sondhi, and V. Khemani, Many-body physics in the nisq era: Quantum programming a discrete time crystal, *PRX Quantum* **2**, 030346 (2021).
 - [13] S. Thanasilp, J. Tangpanitanon, M.-A. Lemonde, N. Dangniam, and D. G. Angelakis, Quantum supremacy and quantum phase transitions, *Phys. Rev. B* **103**, 165132 (2021).
 - [14] P. Frey and S. Rachel, Realization of a discrete time crystal on 57 qubits of a quantum computer, *Science Advances* **8**, eabm7652 (2022), <https://www.science.org/doi/pdf/10.1126/sciadv.abm7652>.
 - [15] W. Xia, J. Zou, X. Qiu, and X. Li, The reservoir learning power across quantum many-body localization transition, *Frontiers of Physics* **17**, 33506 (2022).
 - [16] A. Hayashi, A. Sakurai, S. Nishio, W. J. Munro, and K. Nemoto, Impact of the form of weighted networks on the quantum extreme reservoir computation, *Phys. Rev. A* **108**, 042609 (2023).
 - [17] T. Kubota, Y. Suzuki, S. Kobayashi, Q. H. Tran, N. Yamamoto, and K. Nakajima, Temporal information processing induced by quantum noise, *Phys. Rev. Res.* **5**, 023057 (2023).
 - [18] J. Dambre, D. Verstraeten, B. Schrauwen, and S. Massar, Information processing capacity of dynamical systems, *Scientific Reports* **2**, 514 (2012).
 - [19] R. Martínez-Peña, J. Nokkala, G. L. Giorgi, R. Zambrini, and M. C. Soriano, Information processing capacity of spin-based quantum reservoir computing systems, *Cognitive Computation* **15**, 1440 (2023).
 - [20] J. García-Beni, G. L. Giorgi, M. C. Soriano, and R. Zambrini, Scalable photonic platform for real-time quantum reservoir computing, *Phys. Rev. Appl.* **20**, 014051 (2023).
 - [21] A. Sakurai, M. P. Estarellas, W. J. Munro, and K. Nemoto, Quantum extreme reservoir computation utilizing scale-free networks, *Phys. Rev. Appl.* **17**, 064044 (2022).
 - [22] A. Peruzzo, J. McClean, P. Shadbolt, M.-H. Yung, X.-Q. Zhou, P. J. Love, A. Aspuru-Guzik, and J. L. O'Brien, A variational eigenvalue solver on a photonic quantum processor, *Nature Communications* **5**, 4213 (2014).
 - [23] K. Mitarai, M. Negoro, M. Kitagawa, and K. Fujii, Quantum circuit learning, *Phys. Rev. A* **98**, 032309 (2018).
 - [24] A. B. Magann, C. Arenz, M. D. Grace, T.-S. Ho, R. L. Kosut, J. R. McClean, H. A. Rabitz, and M. Sarovar, From pulses to circuits and back again: A quantum optimal control perspective on variational quantum algorithms, *PRX Quantum* **2**, 010101 (2021).
 - [25] J. I. Colless, V. V. Ramasesh, D. Dahlen, M. S. Blok, M. E. Kimchi-Schwartz, J. R. McClean, J. Carter, W. A. de Jong, and I. Siddiqi, Computation of molecular spectra on a quantum processor with an error-resilient algorithm, *Phys. Rev. X* **8**, 011021 (2018).
 - [26] A. V. Uvarov, A. S. Kardashin, and J. D. Biamonte, Machine learning phase transitions with a quantum processor, *Phys. Rev. A* **102**, 012415 (2020).
 - [27] M. Larocca, P. Czarnik, K. Sharma, G. Muraleedharan, P. J. Coles, and M. Cerezo, Diagnosing Barren Plateaus with Tools from Quantum Optimal Control, *Quantum* **6**, 824 (2022).
 - [28] V. Havlíček, A. D. Córcoles, K. Temme, A. W. Harrow, A. Kandala, J. M. Chow, and J. M. Gambetta, Supervised learning with quantum-enhanced feature spaces, *Nature* **567**, 209 (2019).
 - [29] A. Abbas, D. Sutter, C. Zoufal, A. Lucchi, A. Figalli, and S. Woerner, The power of quantum neural networks, *Nature Computational Science* **1**, 403 (2021).
 - [30] K. Fujii and K. Nakajima, Harnessing disordered-ensemble quantum dynamics for machine learning, *Phys. Rev. Appl.* **8**, 024030 (2017).
 - [31] K. Nakajima, K. Fujii, M. Negoro, K. Mitarai, and M. Kitagawa, Boosting computational power through spatial multiplexing in quantum reservoir computing, *Phys. Rev. Applied* **11**, 034021 (2019).
 - [32] J. Chen, H. I. Nurdin, and N. Yamamoto, Temporal information processing on noisy quantum computers, *Phys. Rev. Applied* **14**, 024065 (2020).
 - [33] G. Angelatos, S. A. Khan, and H. E. Türeci, Reservoir computing approach to quantum state measurement, *Phys. Rev. X* **11**, 041062 (2021).
 - [34] Y. Suzuki, Q. Gao, K. C. Pradel, K. Yasuoka, and N. Yamamoto, Natural quantum reservoir computing for temporal information processing, *Scientific Reports* **12**, 1353 (2022).
 - [35] R. A. Bravo, K. Najafi, X. Gao, and S. F. Yelin, Quantum reservoir computing using arrays of rydberg atoms, *PRX Quantum* **3**, 030325 (2022).
 - [36] L. Domingo, G. Carlo, and F. Borondo, Optimal quan-

- tum reservoir computing for the noisy intermediate-scale quantum era, *Phys. Rev. E* **106**, L043301 (2022).
- [37] K. Fujii and K. Nakajima, Quantum reservoir computing: a reservoir approach toward quantum machine learning on near-term quantum devices (2020), [arXiv:2011.04890 \[quant-ph\]](https://arxiv.org/abs/2011.04890).
- [38] M. V. Altaisky, Quantum neural network [10.48550/ARXIV.QUANT-PH/0107012](https://arxiv.org/abs/10.48550/ARXIV.QUANT-PH/0107012) (2001).
- [39] S. Gupta and R. Zia, Quantum neural networks, *Journal of Computer and System Sciences* **63**, 355 (2001).
- [40] M. Panella and G. Martinelli, Neural networks with quantum architecture and quantum learning, *International Journal of Circuit Theory and Applications* **39**, 61 (2011), <https://onlinelibrary.wiley.com/doi/pdf/10.1002/cta.619>.
- [41] D. Gottesman, The heisenberg representation of quantum computers (1998), [arXiv:quant-ph/9807006 \[quant-ph\]](https://arxiv.org/abs/quant-ph/9807006).
- [42] Y. LeCun, C. Cortes, and C. J. Burges,.
- [43] D. Aharonov, A simple proof that toffoli and hadamard are quantum universal (2003), [arXiv:quant-ph/0301040 \[quant-ph\]](https://arxiv.org/abs/quant-ph/0301040).
- [44] A. Sawicki and K. Karnas, Universality of single-qudit gates, *Annales Henri Poincaré* **18**, 3515 (2017).
- [45] D. Porras and J. I. Cirac, Effective quantum spin systems with trapped ions, *Phys. Rev. Lett.* **92**, 207901 (2004).
- [46] H. Labuhn, D. Barredo, S. Ravets, S. de Léséleuc, T. Macrì, T. Lahaye, and A. Browaeys, Tunable two-dimensional arrays of single rydberg atoms for realizing quantum ising models, *Nature* **534**, 667 (2016).
- [47] J. Zhang, P. W. Hess, A. Kyprianidis, P. Becker, A. Lee, J. Smith, G. Pagano, I.-D. Potirniche, A. C. Potter, A. Vishwanath, *et al.*, Observation of a discrete time crystal, *Nature* **543**, 217 (2017).
- [48] J. Zhang, G. Pagano, P. W. Hess, A. Kyprianidis, P. Becker, H. Kaplan, A. V. Gorshkov, Z.-X. Gong, and C. Monroe, Observation of a many-body dynamical phase transition with a 53-qubit quantum simulator, *Nature* **551**, 601 (2017).
- [49] S. Choi, J. Choi, R. Landig, G. Kucsko, H. Zhou, J. Isoya, F. Jelezko, S. Onoda, H. Sumiya, V. Khemani, *et al.*, Observation of discrete time-crystalline order in a disordered dipolar many-body system, *Nature* **543**, 221 (2017).
- [50] D. Bluvstein, A. Omran, H. Levine, A. Keesling, G. Semeghini, S. Ebadi, T. T. Wang, A. A. Michailidis, N. Maskara, W. W. Ho, *et al.*, Controlling quantum many-body dynamics in driven rydberg atom arrays, *Science* **371**, 1355 (2021), <https://www.science.org/doi/pdf/10.1126/science.abg2530>.
- [51] X. Mi, M. Ippoliti, C. Quintana, A. Greene, Z. Chen, J. Gross, F. Arute, K. Arya, J. Atalaya, R. Babbush, *et al.*, Time-crystalline eigenstate order on a quantum processor, *Nature* **601**, 531 (2022).
- [52] F. Arute, K. Arya, R. Babbush, D. Bacon, J. C. Bardin, R. Barends, R. Biswas, S. Boixo, F. G. S. L. Brandao, D. A. Buell, B. Burkett, Y. Chen, Z. Chen, B. Chiaro, R. Collins, W. Courtney, A. Dunsworth, E. Farhi, B. Foxen, A. Fowler, C. Gidney, M. Giustina, R. Graff, K. Guerin, S. Habegger, M. P. Harrigan, M. J. Hartmann, A. Ho, M. Hoffmann, T. Huang, T. S. Humble, S. V. Isakov, E. Jeffrey, Z. Jiang, D. Kafri, K. Kechedzhi, J. Kelly, P. V. Klimov, S. Knysh, A. Korotkov, F. Kostritsa, D. Landhuis, M. Lindmark, E. Lucero, D. Lyakh, S. Mandrà, J. R. McClean, M. McEwen, A. Megrant, X. Mi, K. Michielsen, M. Mohseni, J. Mutus, O. Naaman, M. Neeley, C. Neill, M. Y. Niu, E. Ostby, A. Petukhov, J. C. Platt, C. Quintana, E. G. Rieffel, P. Roushan, N. C. Rubin, D. Sank, K. J. Satzinger, V. Smelyanskiy, K. J. Sung, M. D. Trevithick, A. Vainsencher, B. Villalonga, T. White, Z. J. Yao, P. Yeh, A. Zalcman, H. Neven, and J. M. Martinis, Quantum supremacy using a programmable superconducting processor, *Nature* **574**, 505 (2019).
- [53] A. S. Menon and N. Puri, Q-means using variational quantum feature embedding (2021).
- [54] J. Duchi, E. Hazan, and Y. Singer, Adaptive subgradient methods for online learning and stochastic optimization., *Journal of machine learning research* **12** (2011).
- [55] S. Haykin, *Neural networks and learning machines*, 3/E (Pearson Education India, 2009).
- [56] P. Pfeffer, F. Heyder, and J. Schumacher, Hybrid quantum-classical reservoir computing of thermal convection flow, *Phys. Rev. Res.* **4**, 033176 (2022).
- [57] M. Hinsche, M. Ioannou, A. Nietner, J. Haferkamp, Y. Quek, D. Hangleiter, J.-P. Seifert, J. Eisert, and R. Sweke, One t gate makes distribution learning hard, *Phys. Rev. Lett.* **130**, 240602 (2023).
- [58] J. Pathak, Z. Lu, B. R. Hunt, M. Girvan, and E. Ott, Using machine learning to replicate chaotic attractors and calculate Lyapunov exponents from data, *Chaos: An Interdisciplinary Journal of Nonlinear Science* **27**, 121102 (2017), https://pubs.aip.org/aip/cha/article-pdf/doi/10.1063/1.5010300/14614073/121102_1_online.pdf.
- [59] M. Lukoševičius and H. Jaeger, Reservoir computing approaches to recurrent neural network training, *Computer Science Review* **3**, 127 (2009).
- [60] R. Martínez-Peña, G. L. Giorgi, J. Nokkala, M. C. Soriano, and R. Zambrini, Dynamical phase transitions in quantum reservoir computing, *Phys. Rev. Lett.* **127**, 100502 (2021).
- [61] X. Han, Y. Zhao, and M. Small, Revisiting the memory capacity in reservoir computing of directed acyclic network, *Chaos: An Interdisciplinary Journal of Nonlinear Science* **31**, 033106 (2021), https://pubs.aip.org/aip/cha/article-pdf/doi/10.1063/5.0040251/14630971/033106_1_online.pdf.
- [62] P. Mujal, R. Martínez-Peña, G. L. Giorgi, M. C. Soriano, and R. Zambrini, Time-series quantum reservoir computing with weak and projective measurements, *npj Quantum Information* **9**, 16 (2023).
- [63] J. T. Edwards and D. J. Thouless, Numerical studies of localization in disordered systems, *Journal of Physics C: Solid State Physics* **5**, 807 (1972).
- [64] S.-i. Amari, A method of statistical neurodynamics, *Kybernetik* **14**, 201 (1974).
- [65] J. Duchi, E. Hazan, and Y. Singer, Adaptive subgradient methods for online learning and stochastic optimization, *Journal of Machine Learning Research* **12**, 2121 (2011).